Journal of Alzheimer's Disease 61 (2018) 1037–1052
DOI 10.3233/JAD-170509
IOS Press

In Vivo Visualization of Tau Accumulation, Microglial Activation, and Brain Atrophy in a Mouse Model of Tauopathy rTg4510

Ai Ishikawa[a,b], Masaki Tokunaga[a], Jun Maeda[a], Takeharu Minamihisamatsu[a], Masafumi Shimojo[a], Hiroyuki Takuwa[a], Maiko Ono[a], Ruiqing Ni[c], Shigeki Hirano[b], Satoshi Kuwabara[b], Bin Ji[a], Ming-Rong Zhang[a], Ichio Aoki[a], Tetsuya Suhara[a], Makoto Higuchi[a] and Naruhiko Sahara[a,*]

[a]*National Institutes for Quantum and Radiological Science and Technology, Chiba, Japan*
[b]*Department of Neurology, Graduate School of Medicine, Chiba University, Chiba, Japan*
[c]*Institute of Biomedical Engineering/Institute for Pharmaceutical Sciences ETH Zurich, Switzerland*

Accepted 11 October 2017

Abstract.

Background: Tau imaging using PET is a promising tool for the diagnosis and evaluation of tau-related neurodegenerative disorders, but the relationship among PET-detectable tau, neuroinflammation, and neurodegeneration is not yet fully understood.

Objective: We aimed to elucidate sequential changes in tau accumulation, neuroinflammation, and brain atrophy by PET and MRI in a tauopathy mouse model.

Methods: rTg4510 transgenic (tg) mice expressing P301L mutated tau and non-tg mice were examined with brain MRI and PET imaging (analyzed numbers: tg = 17, non-tg = 13; age 2.5∼14 months). As PET probes, [^{11}C]PBB3 (Pyridinyl-Butadienyl-Benzothiazole 3) and [^{11}C]AC-5216 were used to visualize tau pathology and 18-kDa translocator protein (TSPO) neuroinflammation. Tau pathology and microglia activation were subsequently analyzed by histochemistry.

Results: PET studies revealed age-dependent increases in [^{11}C]PBB3 and [^{11}C]AC-5216 signals, which were correlated with age-dependent volume reduction in the forebrain on MRI. However, the increase in [^{11}C]PBB3 signals reached a plateau at age 7 months, and therefore its significant correlation with [^{11}C]AC-5216 disappeared after age 7 months. In contrast, [^{11}C]AC-5216 showed a strong correlation with both age and volume reduction until age 14 months. Histochemical analyses confirmed the relevance of pathological tau accumulation and elevated TSPO immunoreactivity in putative microglia.

Conclusion: Our results showed that tau accumulation is associated with neuroinflammation and brain atrophy in a tauopathy mouse model. The time-course of the [^{11}C]PBB3- and TSPO-PET finding suggests that tau deposition triggers progressive neuroinflammation, and the sequential changes can be evaluated *in vivo* in mouse brains.

Keywords: Neuroinflammation, tau-PET, tauopathy, transgenic mice, TSPO, volumetric MRI

INTRODUCTION

Filamentous tau aggregates are the histopathological hallmark of a group of neurodegenerative disorders including Alzheimer's disease (AD), progressive supranuclear palsy, corticobasal degeneration, and Pick's disease, familial frontotemporal lobar degeneration with underlying tau pathology (FTLD-Tau) collectively referred to as tauopathies [1]. Since the pathogenesis of tau pathology is the stem of these disorders, *in vivo* visualization of tau pathology has the potential to enable an early diagnosis of tauopathy. Recent advances in positron

*Correspondence to: Naruhiko Sahara, Department of Functional Brain Imaging Research, National Institute of Radiological Sciences, National Institute for Quantum and Radiological Science and Technology, Chiba 263-8555, Japan. Tel.: +81 43 206 3251; Fax: +81 43 253 0396; E-mail: sahara.naruhiko@qst.go.jp.

emission tomography (PET) imaging for tauopathy allow us to noninvasively examine the state of tau protein in living human brains [2–7]. Among potential tau PET tracers, ^{11}C-labeled phenyl/pyridinil-butadienyl-benzothiazoles/benzothiazolium 3 ([^{11}C]PBB3), [^{18}F]AV-1451, and [^{18}F]THKs have been used for pre-clinical studies in human brain imaging [6–8]. Among these tracers, PBB3 compound, based on a phenyl/pyridinil-butadienyl-benzothiazoles/benzothiazolium (PBB) backbone compound, selectively binds to β-pleated sheet structures such as neurofibrillary tangles (NFTs), neuropil threads (NTs), and diffuse plaques, although selective binding to NFTs is much higher than the binding to plaques [2]. Moreover, the binding affinity of PBB3 to discrete tau pathologies (e.g., NFTs, NTs, coiled bodies, tufted astrocytes, astrocytic plaques) in diverse tauopathies is higher than that of AV-1451, indicating the utility of PBB3 to capture wide-range tau pathologies [9].

Animal models mimicking salient aspects of diseases should be used for preclinical studies. Indeed, genetic mutations identified in familiar forms of disease have led to the recapitulation of underlying pathological processes in animal models. Moreover, conditional transgenic systems now provide powerful experimental tools for investigating the mechanisms of neurodegenerative diseases and evaluation of therapeutic interventions. Based on this system, researchers have developed the rTg4510 mouse line, thereby recapitulating some aspects of AD. The rTg4510 mouse line is a bigenic mouse model that permits the tetracycline-repressible overexpression of P301L mutant tau protein [10]. This P301L mutation was discovered in FTLD-Tau but not in AD [11]. Expression of tau protein is controlled by the tetracycline transactivator (tTA) transgene under the Ca2+/calmodulin-dependent protein kinase IIα (CaMKIIα) promoter, which leads to tau expression in the forebrain of rTg4510 mice. Intracellular deposition of tau protein was pathologically detected in the cortico-limbic area of rTg4510 mice, reflecting tauopathy with similarities to AD and they developed forebrain atrophy associated with aging [10, 12–16]. Immunohistochemical and biochemical examinations of postmortem rTg4510 brains confirmed that the progression of NFT formation was drastically increased from 4 months to 6 months of age [12, 14, 15, 17]. Recently, advanced *in vivo* brain imaging techniques, including manganese-enhanced magnetic resonance imaging (MRI), arterial spin labeling, amide proton transfer imaging, diffusion tenser imaging, and PET, have enabled us to visualize neuronal dysfunction and pathological tau accumulation in living rTg4510 mice [18–22].

Mounting evidence suggests that NFT formation and neuroinflammation play an important role in the neuronal loss during neurodegenerative processes [23–25]. Notably, the immunosuppressive drug FK506 has attenuated the tau pathology and increased the lifespan of the tau model mouse, suggesting neuroinflammation as a causative factor for the development of tauopathy [26]. The mitochondrial 18-kDa translocator protein (TSPO) is upregulated in activated glia in central nervous system inflammatory diseases including AD [27], and several PET tracers (e.g., (R)-[^{11}C]PK11195, [^{18}F]DPA-714, [^{11}C]PBR28, [^{18}F]FEDAA1106) are available for assessing TSPO expression *in vivo* [28]. As for our PET studies with TSPO radioligands, [^{11}C]DAA1106, and [^{11}C]AC-5216, we have demonstrated that TSPO levels were increased not only in human AD [29], but also in the tauopathy model mouse [30], respectively. These results strongly support the hypothesis that neuroinflammation accelerates tau-induced neurodegenerative processes. However, the temporal sequence of microglial activation and NFT formation as well as brain atrophy remains unclear.

In this study, *in vivo* visualization of tau pathology was conducted in rTg4510 mice by utilizing [^{11}C]PBB3 PET imaging. In parallel, the progression of brain atrophy was cross-sectionally examined by T2-weighted MRI and microglial activation was investigated by [^{11}C]AC-5216 PET. By combining non-invasive PET imaging data with structural neuroimaging data of living rTg4510 mice, the aim of the present study was to elucidate the spaciotemporal relationship among tau accumulation, neurodegeneration and neuroinflammation.

MATERIALS AND METHODS

Mice

rTg4510 mice, tau responder mice, and tTA activator mice were obtained from the University of Florida. A parental mutant tau responder line in the FVB/N strain (Clea Inc., Tokyo, Japan) and a tTA activator line in the 129+ter/SV strain (Clea Inc.) were generated and maintained, respectively. To make a tau responder line expressing the 4R0N isoform of human P301L mutant tau, cDNA was placed downstream of

a tetracycline-operon-responder construct. The tTA activator system was placed downstream of CaMKIIα promoter. Hemizygous mice from each parental line were crossed to produce F1 offspring containing rTg4510 mice [10]. For the present study, non-transgenic (non-tg) mice without any exogenous gene expression were used as control mice. All procedures involving mice were performed with approval of the National Institute of Radiological Sciences Institutional Animal Care and Use Committees.

MRI experiments

Twenty-six mice were scanned at age 2.5–4 months ($n = 4$ rTg4510, $n = 3$ non-tg), 7 months ($n = 3$ rTg4510), 10-11 months ($n = 5$ rTg4510), 12–14 months ($n = 5$ rTg4510, $n = 6$ non-tg). All MRI experiments were performed on a 7.0T horizontal MRI scanner (Magnet: Kobelco and JASTEC, Japan; Console: Bruker Biospin, Germany) with a volume coil for transmission (Bruker Biospin) and a 2-ch phased array surface coil for reception (Rapid Biomedical, Germany). The mice were initially anesthetized with 3.0% isoflurane (Escain, Mylan Japan, Japan), and then anesthetized with 1.5∼2.0% isoflurane and 1 : 5 oxygen/room-air mixture during the MRI experiments. Rectal temperature was continuously monitored by optical fiber thermometer (FOT-M, FISO, Canada) and maintained at 36.5 ± 0.5°C using a heating pad (Rapid Biomedical) and warm air. The first imaging slices were carefully set at the rhinal fissure with reference to the mouse brain atlas [31].

T2-weighted MRI: Transaxial T2-weighted fast spin-echo MR images were acquired using a rapid acquisition with relaxation enhancement (RARE) sequence in the same slice position as the T1-weighted MRI. The imaging parameters were as follows: TR/effective TE = 4,200/36 ms, Fat-Sup = on, NA = 4, RARE factor = 8, number of slices = 13, and scan time = 6 min 43 s. Frequency selective saturation pulses and crusher magnetic field gradients were used for fat suppression.

In vivo PET imaging of mice

PET scans were performed using a microPET Focus 220 animal scanner (Siemens Medical Solutions, Malvern, PA) immediately after intravenous injection of [^{11}C]PBB3 or [^{11}C]AC-5216. MicroPET Focus 220 is designed for rodents and small monkeys, providing 95 transaxial planes 0.815 mm (center-to-center) apart, a 19.0-cm transaxial field-of-view (FOV), and a 7.6-cm axial FOV [32]. Radiosyntheses of [^{11}C]PBB3 and [^{11}C]AC-5216 were described in previous reports [2, 30, 33, 34]. Before PET measurements, a 31-gauge needle with catheter was inserted into the mouse tail vein for injection of [^{11}C]PBB3 (35.4 ± 8.4 MBq, specific radioactivity was 79.4 ± 9.9 GBq/μmol at injection) and [^{11}C]AC-5216 (36.2 ± 3.1 MBq, specific radioactivity was 265.6 ± 60.8 GBq/μmol at injection). After a transmission scan for attenuation correction, a bolus of each ligand was injected, and an emission scan in 3D list mode was carried out for 60 or 90 min, respectively. All list-mode data were sorted into 3D sinograms, and were then Fourier-rebinned into 2D sinograms (60 min frames: 1 min × 10, 5 min × 6, 10 min × 2. 90 min frames: 1 min × 4, 2 min × 8, 5 min × 14). Images were reconstructed with filtered back projection using a Hanning filter with a Nyquist cutoff of 0.5 cycle/pixel.

Image analysis

To define anatomical regions of interest (ROIs), manual segmentation was performed on the T2-weighted MRI in a slice by slice fashion, by three experienced investigators using PMOD® software (ver 3.6, PMOD Technologies Ltd, Zurich, Switzerland). To avoid bias, manual tracing was performed without knowing age and genotype. Brain contours were double-checked by a single investigator to finalize the registration of ROIs. For co-registration with PET images, anatomical ROIs were manually defined on a part of cerebral cortices and dorsal hippocampi (labeled as forebrain in Fig. 1). Regional radioactivities of [^{11}C]PBB3 and [^{11}C]AC-5216 were calculated as standardized uptake value [SUV = injected dose per tissue volume × body weight (g)] and the value of area under the curve (AUC) of the time-activity curves (TAC) in each region from 2 to 30, or 0 to 90 min, respectively. The accumulations of radioligands of [^{11}C]PBB3 and [^{11}C]AC-5216 were estimated by the ratios of AUC values in the forebrain to cerebellum from 0 to 60, or 0 to 90 min, respectively.

Fluorescence staining

In vitro fluorescence staining of mouse brain tissues was performed with PBB3 (8-month-old rTg4510, $n = 2$; 10-month-old rTg4510, $n = 2$; 11-month-old rTg4510, $n = 3$; 14-month-old rTg4510, $n = 1$; 8–11-month-old non-transgenic mice, $n = 4$;

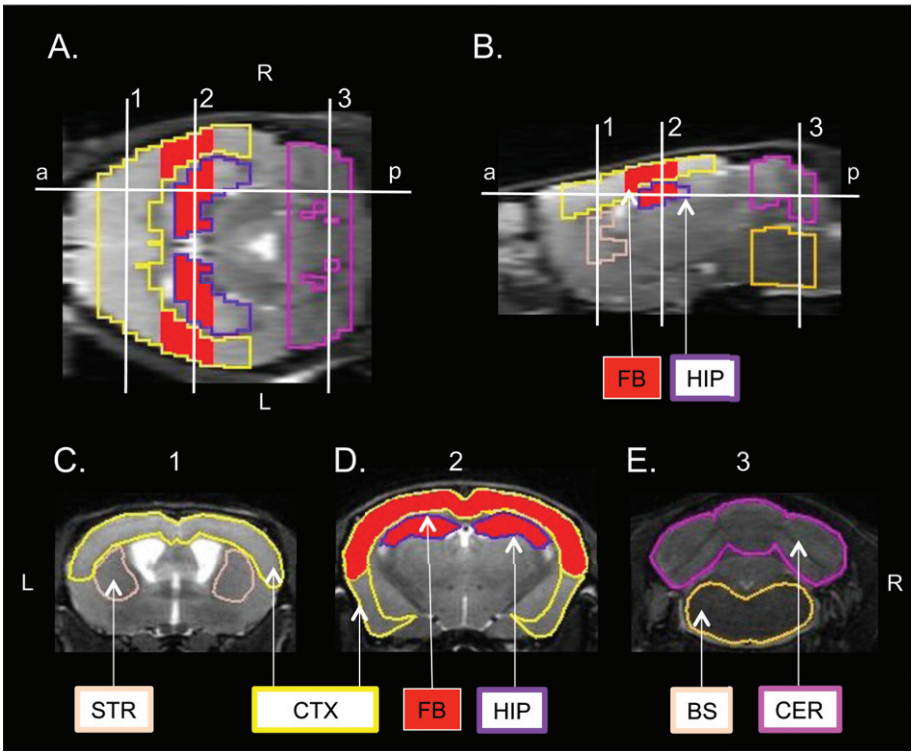

Fig. 1. Anatomical localization of volumes of interest (VOIs). Horizontal (A), sagittal (B), and coronal (C-E) T2W MRI slices of the mouse brain showed six structures: cerebral cortex (CTX), hippocampus (HIP), striatum (STR), cerebellum (CER), brain stem (BS) and forebrain (FB, labeled by red color). The level of the sagittal slice (B) is indicated as a-p line in the horizontal slice (A). Three levels of coronal slices (C-E) are indicated as sagittal sections (1–3). Illustrated brain regions of CER and FB were used for PET quantification. Orientations of slice are indicated as 'a' (anterior), 'p' (posterior), R (right) and L (left).

Table 1
List of rTg4510 mice for histochemical analyses

mouse ID	sex	[^{11}C]PBB3-PET		PBB3-positive cell		[^{11}C]AC-5216-PET		TSPO-positive staining	
		AUC ratio(F/C) %ID/ml	age month	cell number number/0.12 mm^2 field	age month	AUC ratio(F/C) %ID/ml	age month	% % area in 2.5 mm^2 field	age month
TG1	male	1.066	7.56	68	8.29	0.951	7.50	5.57	8.29
TG2	male	1.032	7.56	73	8.29	0.977	7.50	5.72	8.29
TG3	male	1.153	10.19	127	10.49	0.948	10.26	8.63	10.49
TG4	male	1.127	10.42	148	10.49	1.136	10.26	16.5	10.49
TG5	female	1.099	10.39	117	11.11	1.032	10.42	14.6	11.11
TG6	female	1.200	10.39	146	11.11	1.078	10.42	19.8	11.11
TG7	female	1.004	11.34	29	11.51	1.149	11.28	27.4	11.51
TG8	female	1.074	13.71	127	13.91	1.340	13.87	28.4	13.91
NT1	male	0.999	8.58	0	9.04	0.871	8.81	1.83	9.04
NT2	female	1.004	8.52	0	8.98	0.756	8.75	1.53	8.98
NT3	female	0.947	10.39	0	11.10	0.724	10.42	1.83	11.10
NT4	female	0.979	10.29	0	11.00	0.706	10.32	2.56	11.00

Note: ages at PET imaging and sacrifice for brain extraction are aligned.

mouse IDs are listed in Table 1). The fluorescence ligand was dissolved in 50% ethanol. Deparaffinized sections were incubated with 56.5 μM of PBB3 for 30 min at 25°C, followed by washing with 25% ethanol for 5 min. After mounting in non-fluorescent mounting solution (VECTASHIELD, Vector Laboratory, Burlingame, CA), images of fluorescence signals were captured with a Leica microscope (DM4000, Leica, Wetzlar, Germany) equipped with a color digital camera. PBB3-positive cells were manually counted in the field (0.3 mm × 0.4 mm size) of captured images, and

then the number of cells was averaged from 5 fields of each section. For immunohistochemistry, PBB3-stained sections were autoclaved for antigen retrieval. After blocking with TNB blocking solution (PerkinElmer, Waltham, MA), sections were incubated with AT8 (mouse monoclonal, 1 : 500; Thermo Fisher Scientific, Waltham, MA). After incubated with Alexa Fluor 555 goat anti-mouse IgG antibody (1 : 500; Life Technologies, Carlsbad, CA), red fluorescence signals were captured with the same microscope. For co-labeling with AT8 and TSPO, or with TSPO and GFAP, serial sections were incubated with AT8 (1 : 500) and TSPO (rabbit monoclonal, 1 : 1,000; Abcam, Cambridge, UK) antibodies, or with TSPO (1 : 1,000) and GFAP (rat monoclonal, 1 : 500; Zymed, San Francisco, CA) antibodies. For red fluorescence images, Alexa Fluor 555 goat anti-mouse IgG antibody (1 : 500) or Alexa Fluor 555 goat anti-rat IgG antibody (1 : 500) was used. For green fluorescence images, biotinylated goat anti-rabbit IgG (1 : 1,000; Santa Cruz, Dallas, TX) was used for secondary antibody, and immunoreactivity was then visualized using fluorescein-labeled tyramide signal amplification (TSA fluorescein system, PerkinElmer). For co-labeling with TSPO and Iba1 antibodies, sections were first incubated with TSPO antibody (1 : 2,000) followed by incubating with biotinylated goat anti-rabbit IgG (1 : 1,000). After visualizing with TSA fluorescein, sections were incubated with Iba1 antibody (rabbit polyclonal, 1 : 250; Wako, Japan) and labeled with Alexa Fluor 555 goat anti- rabbit IgG antibody (1 : 500). For single labeling with Iba1 or TSPO, serial sections were incubated with Iba1 (1 : 1,000) or TSPO (1 : 1,000). Subsequently, sections were incubated with biotinylated goat anti-rabbit IgG (1 : 1,000), and then visualized using tetramethylrhodamine-labeled tyramide signal amplification (TSA tetramethylrhodamine system). Images were captured by fluorescence microscope (BZ-X700, Keyence, Japan). For image quantification of TSPO-positive signals, multiple images (3×4 images) were captured and stitched into a single image. The area of the TSPO-positive signal was extracted and quantified by BZ-X Analyzer (Keyence). TSPO-positive level was displayed as the signal ratio (%) to the total area (2-3 mm^2 field of forebrain region from each section).

Statistical analysis

Statistical analyses were conducted using PRISM6 (GraphPad Software Inc., La Jolla, CA). Data were analyzed using Spearman's correlation coefficient or nonparametric test for comparing two or more groups, unless otherwise noted. Statistically significance was determined by the *p*-value below 0.05.

RESULTS

Progressive brain atrophy

Mouse brain regional volume was measured by T2-weighted MRI. The five structures—cerebral cortex, hippocampus, striatum, cerebellum, and brain stem—were manually delineated and labeled (Fig. 1). Consistent with previous reports [20, 35], volumetric analysis confirmed prominent brain regional atrophies in hippocampi, cerebral cortices and striata of rTg4510 mouse brains compared to non-tg mice (Fig. 2). In 7- to 14-month-old rTg4510 mice, volume reduction was evident in the cerebral cortex, hippocampus and striatum, whereas volumes in brain stem and cerebellum were intact (Fig. 2B, D-G). On the other hand, volumes of brain regions in 2.5-month-old non-tg mice were not significantly different from those in 12–14-month-old non-tg mice (Fig. 2B-G). Cerebral cortices of 7-, 10-11-, and 12–14-month-old rTg4510 mice were 80%, 53%, and 50% of those of non-tg mice, respectively. Likewise, forebrains of 7-, 10-11-, and 12–14-month-old rTg4510 mice were 72%, 58%, and 51% of those of non-tg mice, respectively. Therefore, atrophy of the forebrain region progressed at a similar rate to cortical volume reduction (Fig. 2C). Although the expression of human tau and the accumulation of pathological tau in the cerebellum and brain stem of rTg4510 mice were sparse, these volumes in 12–14-month-old rTg4510 mice were significantly lower than those in age-matched non-tg mice (brainstem: 90%, cerebellum: 90%) (Fig. 2E, G). These volume reductions were much smaller than those of the other brain regions (cerebral cortex: 50%, hippocampus: 51%, striatum: 53%) (Fig. 2B, D, F). Nevertheless, if tau pathology appeared in the cerebellum and brain stem of 12–14-month-old rTg4510 mice, transmission of tau pathology from forebrain regions might be involved in the volume reductions in these brain regions. However, further investigation will be required to prove this hypothesis.

[^{11}C]PBB3-PET imaging of rTg4510 mice

[^{11}C]PBB3-PET imaging was examined in 2.5–14-month-old rTg4510 mice, which are known to

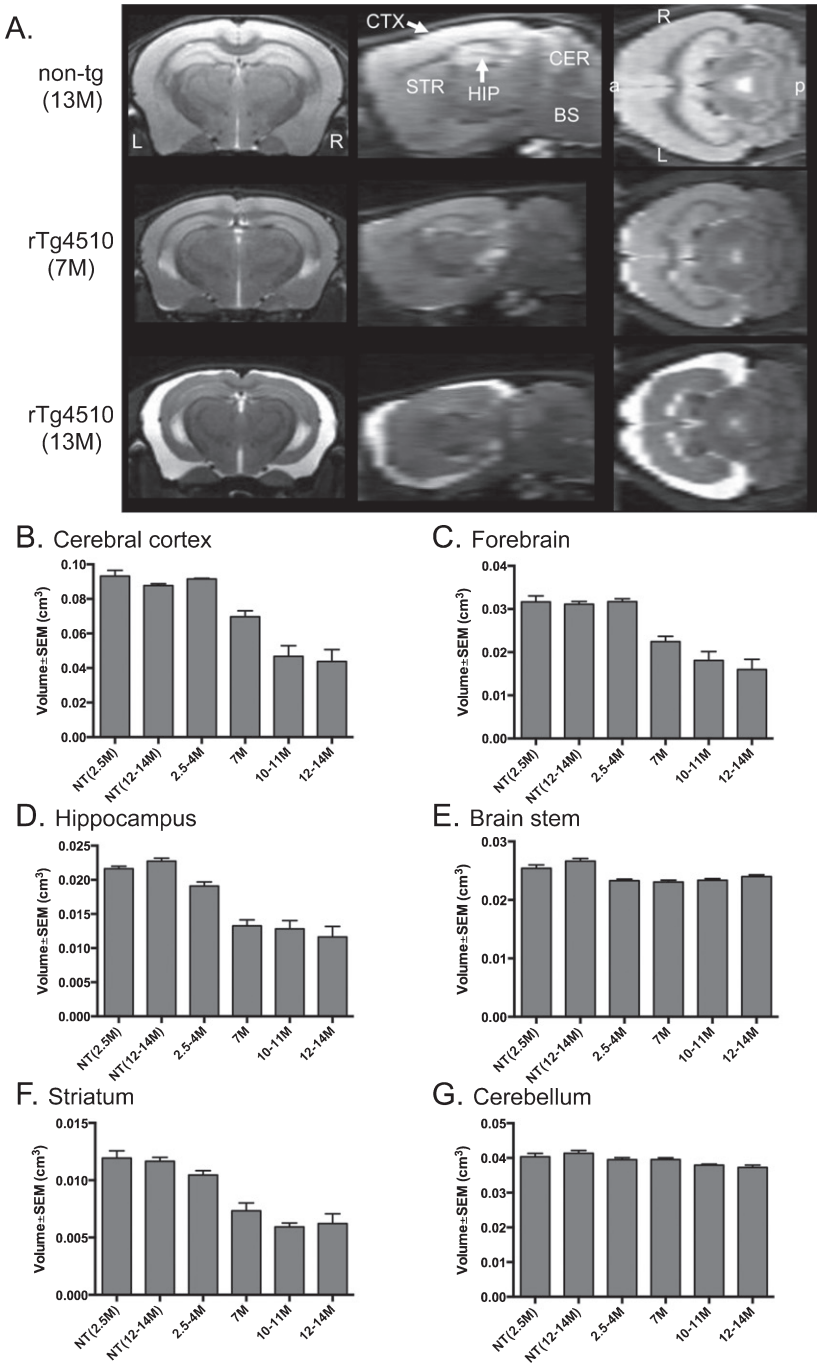

Fig. 2. T2-weighted MRI-based brain volumes of non-tg and rTg4510 mice. A) Representative MR images of 13-month-old non-tg, 7-month-old and 13-month-old rTg4510 mouse brains with coronal, sagittal and horizontal slices. Brain regions of cerebral cortex (CTX), hippocampus (HIP), striatum (STR), cerebellum (CER), and brain stem (BS) are labeled in the sagittal slice of non-tg mice. Orientations of slice are indicated as 'a' (anterior), 'p' (posterior), R (right) and L (left). B-G. Brain volumes of cerebral cortex (B), forebrain (C), hippocampus (D), brain stem (E), striatum (F) and cerebellum (G) from 2.5-month-old non-tg ($n=3$), 12–14-month-old non-tg ($n=6$), 2.5–4-month-old ($n=4$), 7-month-old ($n=3$), 10-11-month-old ($n=5$), and 12–14-month-old ($n=5$) rTg4510 mice. Values are mean ± standard error.

develop tau pathology mostly in the cerebral cortex and hippocampus. After intravenous administration of [^{11}C]PBB3 into rTg4510 mice, unbound [^{11}C]PBB3 was rapidly washed out from the brain, with a half-life of ~10 min, and the radioactivity level reached equilibrium [2]. High [^{11}C]PBB3 binding was observed in the cerebral cortex and hippocampus, and lowest binding in the cerebellum of rTg4510 mice (Fig. 3A), while [^{11}C]PBB3 signal in each brain region of non-tg mice was less than that in the cerebellum of rTg4510 mice (Fig. 3B). When the TAC of [^{11}C]PBB3 signals in each brain region of 12–14-month-old rTg4510 mice ($n = 5$) was compared with that in the same region of age-matched non-tg mice ($n = 6$), significant difference was observed in the forebrain, cerebral cortex, hippocampus, and striatum, but not in the cerebellum and brain stem (Fig. 3C, D and Supplementary Figure 1). The AUC of TAC of [^{11}C]PBB3 signals at 2–30 min in the forebrain of 12–14-month-old rTg4510 mice was significantly higher than that in age-matched non-tg mice, while the difference in the cerebellum between rTg4510 and non-tg mice or the difference between cerebellum and forebrain in rTg4510 mice was not significant (Fig. 3E). Because P301L human tau was neither expressed nor accumulated in the cerebellum of rTg4510 mice [10, 16], the cerebellum was used as a reference region for analyzing the target-to-reference ratio. As a result, the mean forebrain-to-cerebellum ratio of AUC at 0–60 min in 12–14-month-old rTg4510 mice was 9.5% higher than that in age-matched non-tg mice (Fig. 3F; AUC ratio ± SEM in 12–14-month-old rTg4510 mice, 1.06 ± 0.0139; AUC ratio ± SEM in 12–14-month-old non-tg mice, 0.968 ± 0.0143). In rTg4510 mice, the mean AUC ratio increased from 2.5 to 14 months old (Fig. 3G; $n = 17$, $r = 0.56$, $p = 0.022$ by Spearman's correlation analysis). Correlation analysis showed that the [^{11}C]PBB3 level in the forebrain was correlated with the degree of atrophy in the forebrain (Fig. 3H; 2.5–14-month-old rTg4510, $n = 17$, $r = -0.73$, $p = 0.0012$ by Spearman's correlation analysis). It should be noted that the correlation between the AUC ratio of [^{11}C]PBB3 in the forebrain and the volume of the cerebral cortex disappeared when data from over 7 months old were examined (Supplementary Figure 2; 7–14-month-old rTg4510, $n = 13$, $r = -0.51$, $p = 0.081$ by Spearman's correlation analysis). Since volume reduction of the forebrain was concurrent with neuronal loss, it is possible that the disappearance of PBB3-positive neurons canceled the increase of [^{11}C]PBB3 uptake in aged rTg4510 mice.

[^{11}C]AC-5216-PET imaging of rTg4510 mice

PET images of non-tg mice generated by averaging dynamic scan data showed that intravenously administered [^{11}C]AC-5216 labeled the cerebellum and brain stem (Fig. 4B). In line with the previous study [30], levels of [^{11}C]AC-5216 signals in the hippocampus and cerebral cortex were lower than those in the cerebellum, and the striatum was the lowest region of non-tg brains (Fig. 4B). On the other hand, levels of [^{11}C]AC-5216 signals in the hippocampus and cerebral cortex of 12–14-month-old rTg4510 mice were higher than those of age-matched non-tg mice (Fig. 4A, B). The retention of [^{11}C]AC-5216 in the striatum of rTg4510 mice was slightly higher than that in the cerebellum (Fig. 4A). The TAC of [^{11}C] AC-5216 signals further confirmed higher retention of [^{11}C] AC-5216 in the forebrain, hippocampus, cerebral cortex, and striatum of 12–14-month-old rTg4510 mice ($n = 5$) than in the same regions of age-matched non-tg mice ($n = 6$) (Fig. 4 C and Supplementary Figure 3). Although previous work used the striatum as a reference region [30], we had to abandon this method in the current study because of the striatal accumulation in rTg4510 mice. In contrast, the cerebellum of rTg4510 mice showed a lack of human P301L tau expression and a lower level of [^{11}C]AC-5216 signal than other brain regions (Fig. 4A, D, E, and Supplementary Figure 3A-D). The brain stem of rTg4510 mice was another brain region with less human P301L tau expression, but the TAC in this region showed slower clearance of unbound [^{11}C]AC-5216 than that in the cerebellum (Fig. 4D and Supplementary Figure 3D). Therefore, the cerebellum was selected as reference region to estimate AUC of [^{11}C]AC-5216 signals in the subsequent analyses. Similar to [^{11}C]PBB3-PET, AUC of [^{11}C]AC-5216 signals from 0 to 90 min in forebrain of 12–14-month-old rTg4510 mice was significantly higher than those in age-matched non-tg mice (Fig. 4E). The difference in forebrain was much greater than the difference in cerebellum (Fig. 4E), with the mean forebrain-to-cerebellum ratio of AUC at 0–90 min in 12–14-month-old rTg4510 mice being 61% higher than that in age-matched non-tg mice (Fig. 4F; AUC ratio ± SEM in 12–14-month-old rTg4510 mice, 1.21 ± 0.0842; AUC ratio ± SEM in 12–14-month-old non-tg mice, 0.750 ± 0.0227). This AUC ratio in rTg4510 mice continued to increase with age (Fig. 4G; $n = 17$, $r = -0.85$, $p < 0.0001$ by Spearman's correlation analysis). Correlation analysis showed that the [^{11}C]AC-5216 AUC ratio in

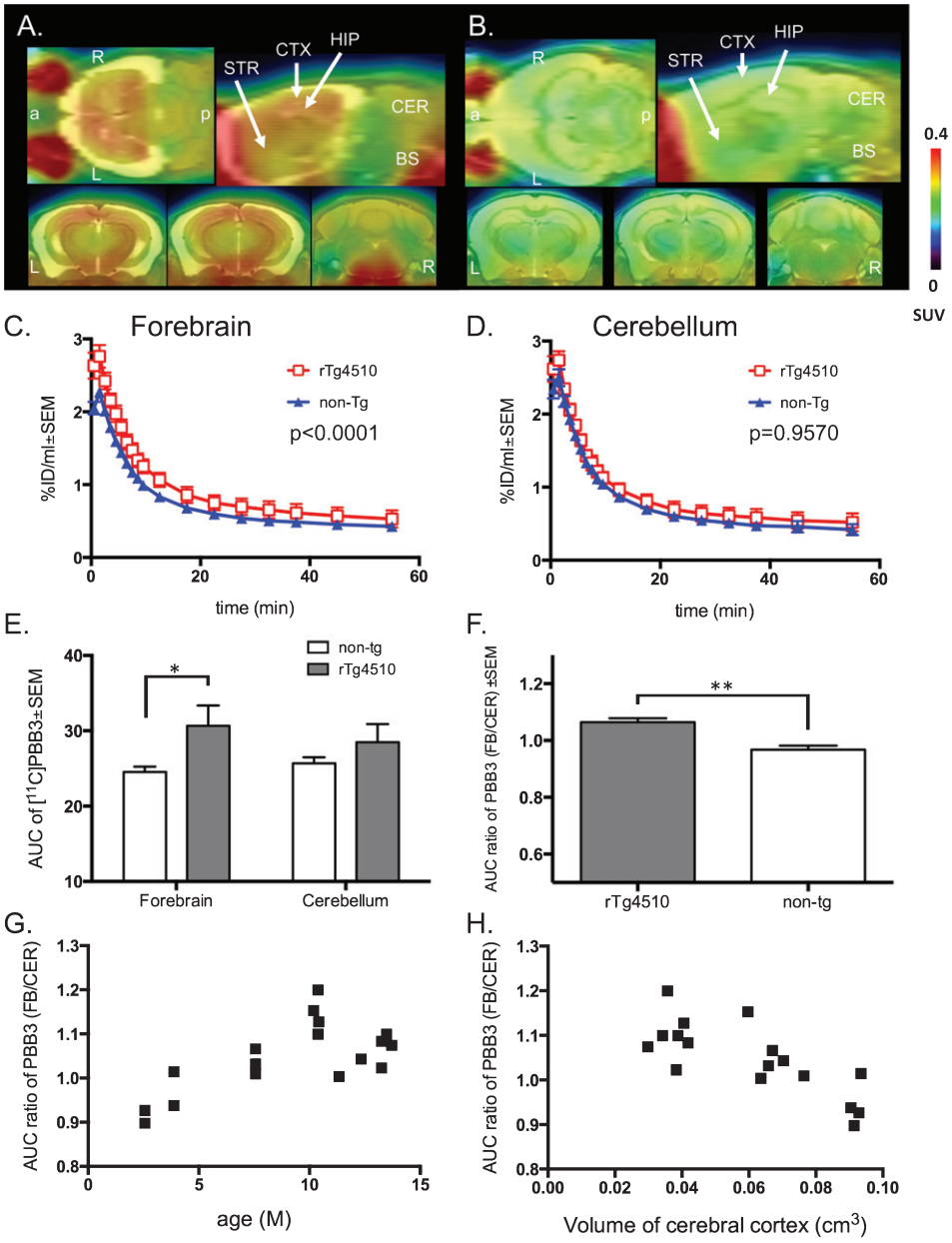

Fig. 3. Accumulation of [^{11}C]PBB3 signals in rTg4510 mouse brains. A,B) Orthogonal views of [^{11}C]PBB3 PET images in brains of 13-month-old rTg4510 (A) and 13-month-old non-tg (B) mice generated by averaging dynamic scan data at 0–60 min after intravenous injection of [^{11}C]PBB3. Images indicated as horizontal (upper left), sagittal (upper right), dorsal hippocampal level of coronal (left), ventral hippocampal level of coronal (middle) and cerebellum level of coronal (right) slices. Brain regions of cerebral cortex (CTX), hippocampus (HIP), striatum (STR), cerebellum (CER), and brain stem (BS) are labeled in the sagittal slice. Orientations of slice are indicated as 'a' (anterior), 'p' (posterior), R (right) and L (left). C,D) Time-radioactivity curves in the forebrain (C) and cerebellum (D) in 12-14-month-old non-tg (blue triangles, $n=6$) and rTg4510 (red squares, $n=5$) mice. Error bars represent SEM. The difference in the forebrain between rTg4510 and non-tg was significant (interaction p value <0.0001 by two-way ANOVA), but not in the cerebellum (interaction p value $=0.96$ by two-way ANOVA). E. Mean AUC at 2–30 min in the forebrain or the cerebellum of 12–14-month-old non-tg (open columns, $n=6$) and rTg4510 (filled columns, $n=5$) from dynamic PET scans. Error bars represent SEM. Mean AUC in the forebrain of rTg4510 mice was significantly higher than that in the forebrain of non-tg mice ($^{*}p<0.05$ by independent t-test), whereas the difference in the cerebellum was not significant. F. AUC ratio (forebrain to cerebellum) at 0–60 min of 12–14-month-old rTg4510 (filled columns, $n=5$) and non-tg (open columns, $n=6$). Error bars represent SEM. AUC ratio of rTg4510 mice was significantly higher than that of non-tg mice ($^{**}p<0.01$) G. Scatterplot of AUC ratio (forebrain to cerebellum) for [^{11}C]PBB3 against age (months) of rTg4510 mice ($n=17$). H. Scatterplot of AUC ratio (forebrain to cerebellum) for [^{11}C]PBB3 against neocortical volume (cm^3) of rTg4510 mice ($n=17$).

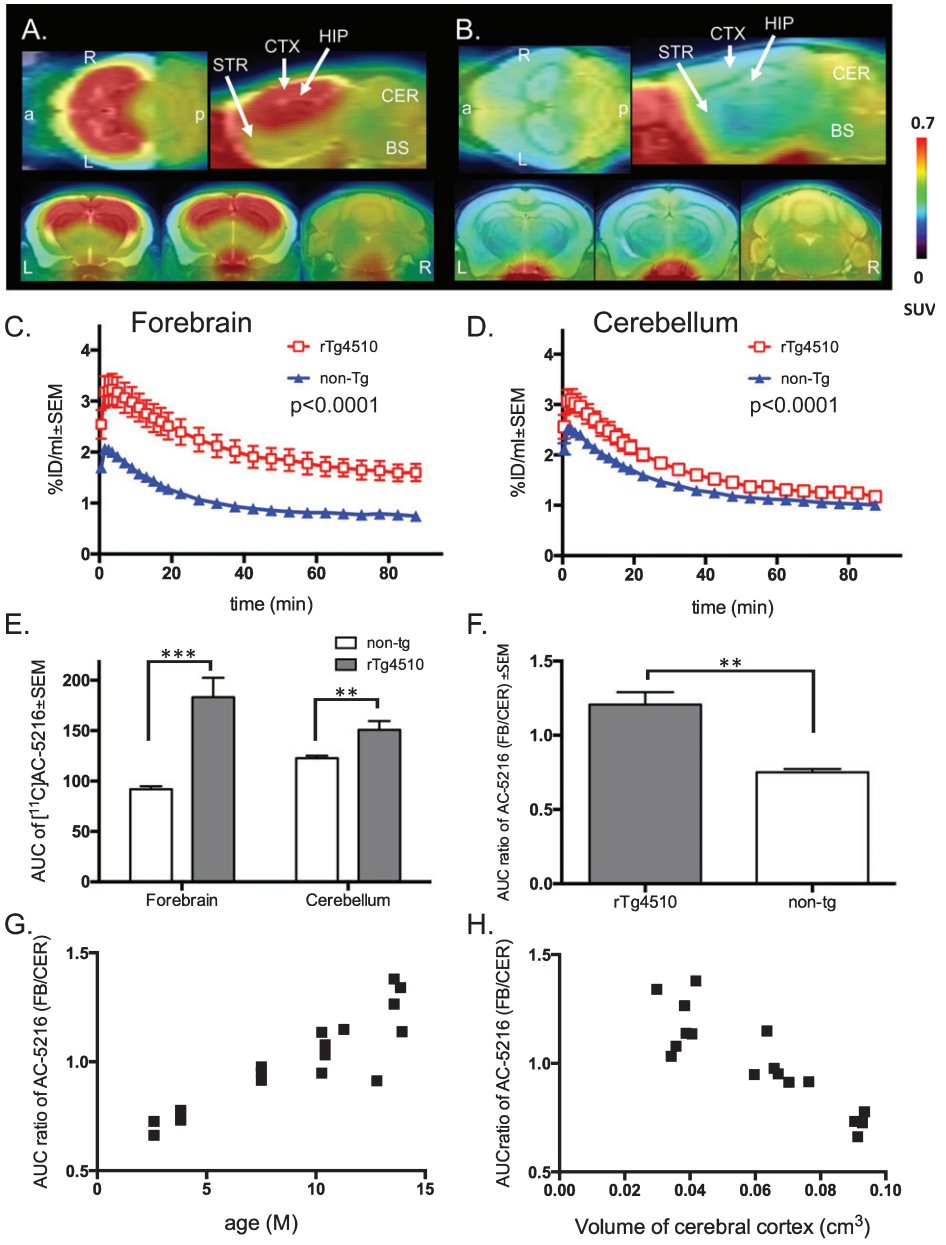

Fig. 4. Progression of microglial activation visualized by [^{11}C]AC-5216 PET imaging in rTg4510 mouse brains. A,B) Orthogonal views of TSPO distribution in brains of 13-month-old rTg4510 (A) and 13-month-old non-tg (B) mice generated by averaging dynamic scan data at 0–90 min after intravenous injection of [^{11}C]AC-5216. Images indicated as horizontal (upper left), sagittal (upper right), dorsal hippocampal level of coronal (left), ventral hippocampal level of coronal (middle) and cerebellum level of coronal (right) slices. Brain regions, cerebral cortex (CTX), hippocampus (HIP), striatum (STR), cerebellum (CER), brain stem (BS) are labeled in the sagittal slice. Orientations of slice are indicated as 'a' (anterior), 'p' (posterior), R (right) and L (left). C,D) Time-radioactivity curves in the forebrain (C) and cerebellum (D) in 12–14-month-old non-tg (blue triangles, $n=6$) and rTg4510 (red squares, $n=5$) mice. Error bars represent SEM. The differences in the forebrain and cerebellum between rTg4510 and non-tg were significant (interaction p value <0.0001 by two-way ANOVA). E. Mean AUC at 0–90 min in the forebrain or the cerebellum of 12–14-month-old non-tg (open columns, $n=6$) and rTg4510 (filled columns, $n=5$) from dynamic PET scans. Error bars represent SEM. Mean AUC in rTg4510 mice was significantly higher than that in non-tg mice ($^{***}p<0.001$ by independent t-test for the forebrain, $^{**}p<0.01$ by independent t-test for the cerebellum). F. AUC ratio (forebrain to cerebellum) at 0–90 min of 12–14-month-old rTg4510 (filled columns, $n=5$) and non-tg (open columns, $n=6$). Error bars represent SEM. AUC ratio of rTg4510 mice was significantly higher than that of non-tg mice ($^{**}p<0.01$) G. Scatterplot of AUC ratio (forebrain to cerebellum) for [^{11}C]AC-5216 against age (months) of rTg4510 mice ($n=17$). H. Scatterplot of AUC ratio (forebrain to cerebellum) for [^{11}C]AC-5216 against neocortical volume (cm^3) of rTg4510 mice ($n=17$).

A.

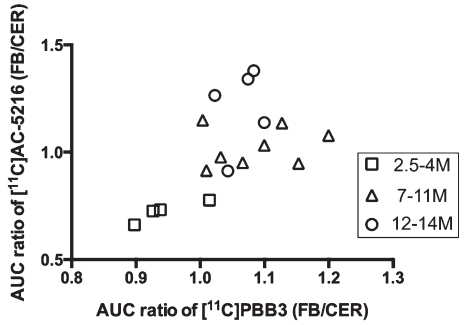

B.

AC-5216 vs. PBB3

Parameter	2.5-14M	2.5-11M	7-14M
Number	17	12	13
Spearman's r	0.5392	0.6503	0.03297
P value (two-tailed)	0.0275	0.0257	0.921
P value summary	*	*	ns

Fig. 5. Correlation between [^{11}C]AC-5216 and [^{11}C]PBB3 signals in forebrains of rTg4510 mice. A. Scatterplot of AUC ratio (forebrain to cerebellum) for [^{11}C]AC-5216 of rTg4510 mice against AUC ratio (forebrain to cerebellum) for [^{11}C]PBB3. 2.5–4-month-old ($n=4$, squares), 7–11-month-old ($n=8$, triangles) and 12–14-month-old ($n=5$, circles) rTg4510 mice were presented in the plot. B. Statistical data showing the correlation between [^{11}C]AC-5216 and [^{11}C]PBB3 signals. Spearman's correlation analysis was performed. Significant correlation was found: $^{*}p<0.05$.

the forebrain was negatively correlated with the volume of the cerebral cortex (Fig. 4H; $n=17$, $r=-0.83$, $p<0.0001$ by Spearman's correlation analysis).

Linkage between tau pathology and microglia activation

Since both [^{11}C]PBB3 and [^{11}C]AC-5216 levels were significantly correlated with age and brain atrophy, we next examined the relationship between [^{11}C]PBB3 and [^{11}C]AC-5216 levels, and we found a positive correlation (Fig. 5; 2.5–14-month-old rTg4510, $n=17$, $r=0.54$, $p=0.028$ by Spearman's correlation analysis). This correlation was also significant when the age range of 2.5 to 11 months was selected (Fig. 5; 2.5–11-month-old, $n=12$, $r=0.65$, $p=0.026$ by Spearman's correlation analysis). In contrast, the correlation between [^{11}C]PBB3 and [^{11}C]AC-5216 signals disappeared when the age range of 7 to 14 months was chosen, likely due to the saturation of [^{11}C]PBB3 signals in rTg4510 mice over 7 months of age (Fig. 5; 7–14-month-old, $n=13$, $r=0.033$, $p=0.92$ by Spearman's correlation analysis).

Our previous study and the current data showed that fluorescence labeling with PBB3 for brain sections of rTg4510 mice provided evidence of PBB3-binding neuronal inclusions in the cerebral cortex and hippocampus of aged rTg4510 mice (Fig. 6A, 7C) [2]. This evidence strongly supported the viewpoint that *in vivo* [^{11}C]PBB3-PET imaging demonstrated the amount of tau inclusions in living brains. On the other hand, the feasibility of [^{11}C]AC-5216 for TSPO was examined in detail [36], and [^{11}C]AC-5216-PET imaging most likely expressed the amount of TSPO in response to microglial activation (Fig. 6B). To validate the *in vivo* evidence, brain dissection after *in vivo* imaging followed by histochemical analysis was performed. As shown in Fig. 6, PBB3-positive neurons were co-labeled with AT8 antibody in the cerebral cortex of 14-month-old rTg4510 mice, indicating the existence of PBB3-positive hyperphosphorylated tau accumulation in neurons (Fig. 6A). On the other hand, TSPO immunoreactivity was co-labeled with microglia marker Iba1 antibody but not co-localized with AT8-positive neurons (Fig. 6B, C). TSPO signals were not overlapped with GFAP signals, suggesting that TSPO was rarely expressed in astrocytes (Fig. 6D). Quantitative analysis of PBB3 fluorescence staining confirmed the positive correlation between PBB3-positive cell count and the AUC ratio of [^{11}C]PBB3 (Table 1 and Fig. 7A; $n=8$, $r=0.81$, $p=0.022$ by Spearman's correlation analysis). Similarly, the immunoreactivity of the TSPO signal was positively correlated with the AUC ratio of [^{11}C]AC-5216 (Table 1 and Fig. 7B; $n=8$, $r=0.90$, $p=0.0046$ by Spearman's correlation analysis). In the non-tg cerebral cortex, there was no PBB3-labeled inclusion and faint TSPO-positive immunoreactivity (Fig. 7A, B). Representative histochemical images showed that most of PBB3-positive neurons were co-labeled with AT8 antibody in rTg4510 cerebral cortices (Fig. 7C). As confirmed by the correlation analysis, mice with more PBB3- and AT8-positive neurons (TG3 and TG4) showed a higher level of the AUC ratio of [^{11}C]PBB3 (Fig. 7A). Accumulation of TSPO immunoreactivity was observed in two rTg4510 mice (TG4 and TG7) with a higher AUC ratio of [^{11}C]AC-5216 (Fig. 7B). Because both TSPO- and microglial marker Iba1-positive signals were increased with age and were higher than in non-tg mice (Fig. 7D), age-dependent and tau-induced microglial activation was evident in rTg4510 mice. Taken together, our data strongly supported the utility of [^{11}C]PBB3-PET and [^{11}C]AC-5216 for the *in*

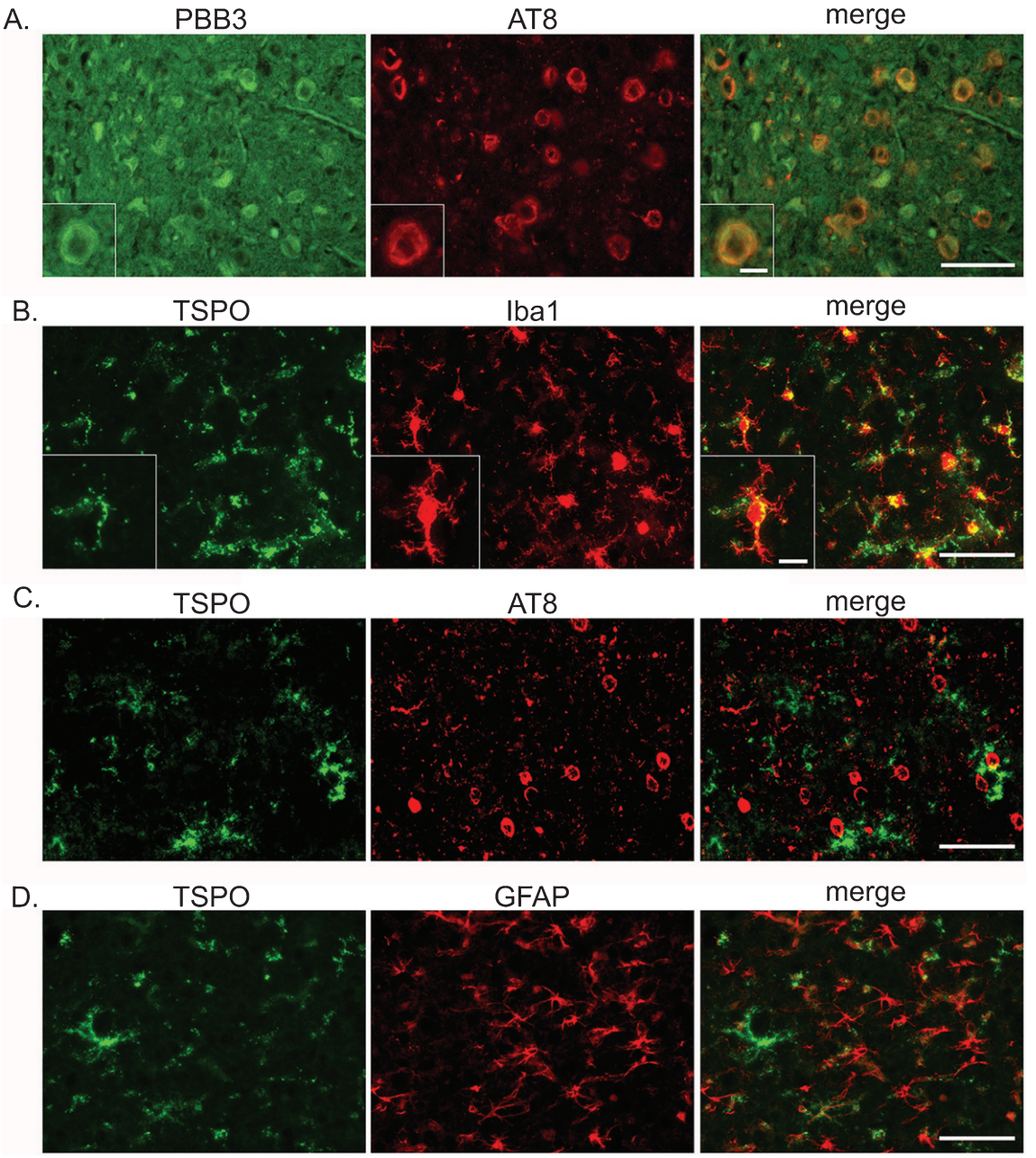

Fig. 6. PBB3 fluorescence labeling and immunohistochemistry. Sagittal serial sections of 14-month-old rTg4510 mouse were labeled with PBB3 and several antibodies. A) Representative image of co-labeling with PBB3 (green) and AT8 (red) antibody in cerebral cortex of rTg4510 mice. Image of PBB3 labeling was captured by Leica fluorescence microscope. Image-captured section was re-labeled with AT8 antibody, and then the identical field was captured with red fluorescence filter. Scale bars = 50 μm and 10 μm (inset). B) Representative image of double-staining with TSPO (green) and Iba (red) antibodies in cerebral cortex of rTg4510 mice. C) Representative image of double-staining with TSPO (green) and AT8 (red) antibodies in cerebral cortex of rTg4510 mice. D) Representative image of double-staining with TSPO (green) and GFAP (red) antibodies in cerebral cortex of rTg4510 mice. Images of B-D were captured by Keyence microscope. Scale bars = 50 μm and 10 μm (inbox).

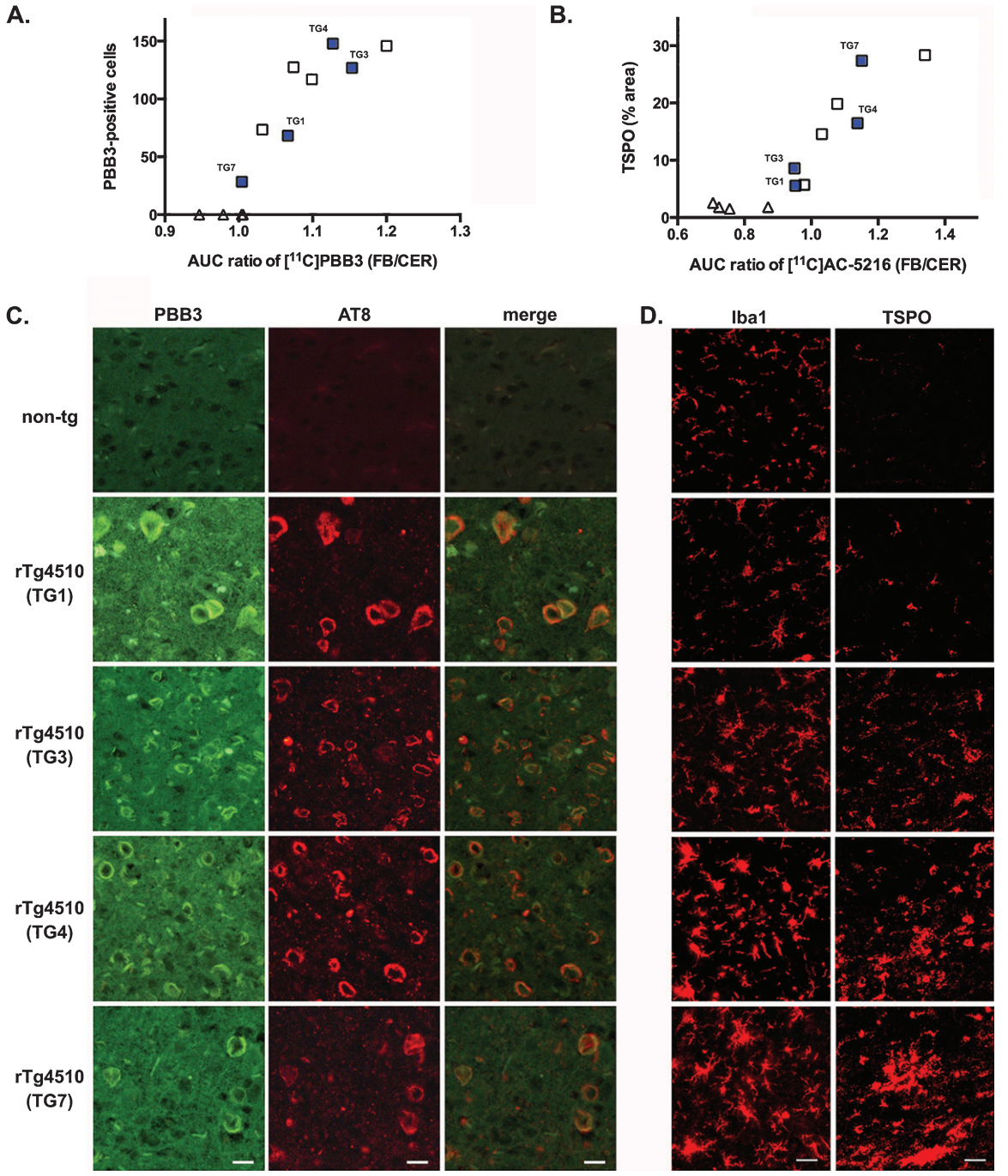

Fig. 7. Correlation between histology and PET. A) Scatterplot of PBB3-positive cell numbers in cerebral cortices of rTg4510 and non-tg mice ($n = 8$, squares, TG1-TG8; $n = 4$, triangles, NT1-NT4 listed in Table 1) against AUC ratio (forebrain to cerebellum) for [^{11}C]PBB3. PBB3-positive cell numbers were averaged in five fields of PBB3 fluorescence-labeled images (0.3 mm × 0.4 mm). B) Scatterplot of TSPO immunoreactivities in forebrains of rTg4510 and non-tg mice ($n = 8$, squares, TG1-TG8; $n = 4$, triangles, NT1-NT4 listed in Table 1) against AUC ratio (forebrain to cerebellum) for [^{11}C]AC-5216. Immunoreactivity was presented as a signal ratio (%) in total area (2.5 mm^2 field of forebrain region). C) Representative images of co-labeling with PBB3 (green) and AT8 (red) antibody in cerebral cortices of 9-month-old non-tg, 8-month-old (TG1), 10.5-month-old (TG3 and TG4) and 11-month-old (TG7) rTg4510 mice. Images were captured by Leica fluorescence microscope. Scale bars = 20 μm. D. Representative images of immunohistochemistry. Cerebral cortices in sagittal serial sections of 9-month-old non-tg, 8-month-old (TG1), 10.5-month-old (TG3 and TG4) and 11-month-old (TG7) rTg4510 mice were labeled with Iba1 (red) and TSPO (red) antibodies. Images were captured by Keyence microscope. Scale bar = 20 μm.

vivo visualization of tau pathology and neuroinflammation in rTg4510 mice, respectively.

DISCUSSION

In the present study, we demonstrated PET and MRI of transgenic mice modeling tauopathy and non-tg controls in order to examine the utility of small-animal *in vivo* imaging for pursuing links between tau deposition and neurodegeneration. Along with [^{11}C]PBB3, microglial activation was also visualized in rTg4510 mice using a radioligand for TSPO, [^{11}C]AC-5216. In rTg4510 mice, tau accumulation, neuroinflammation, and neocortical atrophy became noticeable at 7 months of age, and retentions of tau and TSPO radioligands were inversely correlated to neocortical volumes (Figs. 3 and 4). Postmortem immunohistochemical assays revealed that both tau deposition and elevated TSPO signals in putative microglia were strongly associated with PET signals in the neocortex of rTg4510 mice (Fig. 7). Our results indicate that the temporal relationship among tau deposition, neuroinflammation and neuronal loss can be pursued by *in vivo* imaging of animal models.

Our [^{11}C]PBB3 PET imaging of rTg4510 mice showed that the [^{11}C]PBB3 signal reached a plateau by 7 months of age (Fig. 3G). Previous studies using immunohistochemistry and biochemical assays have shown a prominent increase and a good correspondence of PBB3 signals with tau levels stained by several tau antibodies (e.g., PHF1, Ab39, MC1) and Thioflavin-S in the neocortex and hippocampus of rTg4510 mice between 4 and 6 months old and that the levels remained stable after 7 months of age [15, 16, 37–39]. This age-dependent development of tau pathology was in line with *in vivo* PBB3 signals in the current study. We also observed the plateaued tau pathology, which showed no significant difference in [^{11}C]PBB3 levels between 7-month-old and 12–14-month-old rTg4510 mice. Correlation analysis between [^{11}C]PBB3 levels and brain atrophy showed no significance in over 7-month-old rTg4510 mice (Supplementary Figure 2). The lack of correlation of [^{11}C]PBB3 levels from brain atrophy may be due to the disappearance of PBB3-positive inclusions with aging. To elucidate this possibility, *in vivo* two-photon microscopic imaging is currently being performed to investigate the progression of tau pathology at cellular levels (manuscript in preparation). If longitudinal monitoring can verify both production and disappearance of PBB3-positive neurons, the actual amount of PBB3-positive tau inclusions may not reflect the total production but rather the total in-out balance of tau inclusions. Of interest is the question of whether the production rate of PBB3-positive inclusions is strongly associated with the severity of neuronal impairments. Further studies in live animals are necessary for estimation of the production speed of PBB3-positive inclusions.

Since PBB3 selectively binds to β-pleated sheet structures such as NFTs, but not to pre-tangles and/or immature tau aggregates, results from [^{11}C]PBB3 PET regarding rTg4510 tau pathology likely represent the accumulation of NFTs (i.e., mature tau aggregates). Although the abundance of NFTs is positively correlated with the severity of cognitive deficits in AD [40, 41], accumulating evidence from the study of mechanisms of tau-induced neurotoxicity indicated that pre-fibrillar tau aggregates, but not NFTs, might cause neuronal dysfunction. Therefore, detection of [^{11}C]PBB3 signal may in fact not reflect tau-induced neurotoxicity. However, in combination with volumetric MRI and [^{11}C]AC-5216 PET, [^{11}C]PBB3 PET imaging is useful for diagnosing neurodegeneration in a mouse model of tauopathy.

Inflammation has been suggested as playing a key role in regulating both amyloid and tau pathology (reviewed in [42, 43]). Chronic treatment of lipopolysaccharide (LPS) in the 3xTg mouse model confirmed that neuroinflammatory cytokines and reactive microglia exacerbate the tau pathology and contribute to the spreading of tau [44, 45]. According to these observations, the development of tau pathology was triggered by increased tau phosphorylation. Although tau phosphorylation seems to be essential for NFT formation, LPS treatment may not be enough to develop into tau aggregation. Likewise, acute LPS administration into rTg4510 mice induced tau phosphorylation while tau aggregation was not affected [46]. In the present study, elevated [^{11}C]AC-5216 signals in the forebrain of rTg4510 mice appeared at 7 months of age (Fig. 4E). Neither Iba1 nor TSPO-labeled microglia were accumulated in younger rTg4510 mice. Since intraneuronal inclusions labeled by tau oligomer-specific antibody appeared as early as at 1.5 months of age [39], neuroinflammatory response may be downstream of the formation of pathological tau aggregates. However, it is still unclear whether microglial activation already occurs before pathological tau accumulation, as this depends on the sensitivity and specificity of both Iba1 and TSPO antibodies for detecting activated

microglia. In contrast to the investigation of inflammatory mechanisms against tau pathology, it has been reported that non-steroidal anti-inflammatory drugs such as γ-secretase modulators influenced the Aβ population. Epidemiological studies have demonstrated a link between the use of anti-inflammatory drugs and the prevalence of AD [47]. Therefore, the induction of pro-inflammatory mediators likely exacerbates the Aβ pathology [48]. Conversely, the activation of glial cells can stimulate clearance of Aβ plaques via the induction of phagocytosis [49]. This would be feasible if the pathogenesis of tau protein is associated with such dual functions of neuroinflammation. Microglial phagocytosis of tau aggregates similar to the clearance of Aβ plaques should be confirmed by examination of *in vivo* fluorescence microscopic imaging, awaiting only the development of a specific fluorescent labeling for microglial cells.

The recent development of Aβ and tau PET ligands will assist in advanced clinical diagnosis of AD. As the next step, early pathological biomarkers will prove essential for effective therapeutic intervention. Since current tau PET tracers have a limitation regarding the detection of pre-fibrillar tau aggregates, novel ligands that potentially recognize pre-fibrillar and/or intermediate aggregated species of tau need to be developed. In fact, our previous study showed that tau oligomer-specific antibody TOC1-positive inclusions preceded PBB3-positive signals using double-fluorescence staining of rTg4510 brain sections [39]. Therefore, the conformation of TOC-1-positive tau likely takes place before PBB3-positive β-sheet-rich structures, although this remains inconclusive in terms of β-sheet specific amyloid tracers in their detection of amyloid oligomers/protofibrils [50]. Because several groups have identified unique chemical compounds that preferentially bind to intermediate aggregates of Aβ and tau [51–55], those compounds might represent more suitable ligands for the early detection of AD pathology.

In conclusion, the utilities of [^{11}C]PBB3 and [^{11}C]AC-5216 for evaluating disease progression in living tauopathy brains were confirmed by *in vivo* imaging of a tauopathy mouse model. The time-course of *in vivo* imaging indicates that the elevated TSPO signal is induced by tau deposition and correlates well with brain atrophy. Our system allows us to non-invasively examine the mechanisms underlying both tau-induced neurodegeneration and neuroinflammation.

ACKNOWLEDGMENTS

We would like to thank Dr. Jada Lewis (University of Florida) for supporting the rTg4510 mouse study; Shouko Uchida and Izumi Matsumoto (National Institute of Radiological Sciences) for technical assistance; and staff of the Molecular Probe Group (National Institute of Radiological Sciences) for support with radiosynthesis. This research was supported in part by grants from Grant-in-Aid for Science Research on Innovation Area ("Brain Protein Aging" 26117001 to N.S.) and Scientific Research (C) (15K06793 to N.S.) from the Ministry of Education, Culture, Sports, Science and Technology, Japan, and from the Strategic Research Program for Brain Sciences from Japan Agency for Medical Research and Development, AMED. M.H. holds a patent on compounds including PBB3 (JP 5422782/EP 12 844 742.3).

Authors' disclosures available online (https://www.j-alz.com/manuscript-disclosures/17-0509r2).

SUPPLEMENTARY MATERIAL

The supplementary information is available in the electronic version of this article: http://dx.doi.org/10.3233/JAD-170509.

REFERENCES

[1] Lee VM, Goedert M, Trojanowski JQ (2001) Neurodegenerative tauopathies. *Annu Rev Neurosci* **24**, 1121-1159.

[2] Maruyama M, Shimada H, Suhara T, Shinotoh H, Ji B, Maeda J, Zhang MR, Trojanowski JQ, Lee VM, Ono M, Masamoto K, Takano H, Sahara N, Iwata N, Okamura N, Furumoto S, Kudo Y, Chang Q, Saido TC, Takashima A, Lewis J, Jang MK, Aoki I, Ito H, Higuchi M (2013) Imaging of tau pathology in a tauopathy mouse model and in Alzheimer patients compared to normal controls. *Neuron* **79**, 1094-1108.

[3] Harada R, Okamura N, Furumoto S, Tago T, Maruyama M, Higuchi M, Yoshikawa T, Arai H, Iwata R, Kudo Y, Yanai K (2013) Comparison of the binding characteristics of [18F]THK-523 and other amyloid imaging tracers to Alzheimer's disease pathology. *Eur J Nucl Med Mol Imaging* **40**, 125-132.

[4] Okamura N, Furumoto S, Harada R, Tago T, Yoshikawa T, Fodero-Tavoletti M, Mulligan RS, Villemagne VL, Akatsu H, Yamamoto T, Arai H, Iwata R, Yanai K, Kudo Y (2013) Novel 18F-labeled arylquinoline derivatives for noninvasive imaging of tau pathology in Alzheimer disease. *J Nucl Med* **54**, 1420-1427.

[5] Chien DT, Bahri S, Szardenings AK, Walsh JC, Mu F, Su MY, Shankle WR, Elizarov A, Kolb HC (2013) Early clinical PET imaging results with the novel PHF-tau radioligand [F-18]-T807. *J Alzheimers Dis* **34**, 457-468.

[6] Ariza M, Kolb HC, Moechars D, Rombouts F, Andres JI (2015) Tau positron emission tomography (PET) imaging: Past, present, and future. *J Med Chem* **58**, 4365-4382.

[7] Villemagne VL, Fodero-Tavoletti MT, Masters CL, Rowe CC (2015) Tau imaging: Early progress and future directions. *Lancet Neurol* **14**, 114-124.

[8] Saint-Aubert L, Lemoine L, Chiotis K, Leuzy A, Rodriguez-Vieitez E, Nordberg A (2017) Tau PET imaging: Present and future directions. *Mol Neurodegener* **12**, 19.

[9] Ono M, Sahara N, Kumata K, Ji B, Ni R, Koga S, Dickson DW, Trojanowski JQ, Lee VM, Yoshida M, Hozumi I, Yoshiyama Y, van Swieten JC, Nordberg A, Suhara T, Zhang MR, Higuchi M (2017) Distinct binding of PET ligands PBB3 and AV-1451 to tau fibril strains in neurodegenerative tauopathies. *Brain* **140**, 764-780.

[10] Santacruz K, Lewis J, Spires T, Paulson J, Kotilinek L, Ingelsson M, Guimaraes A, DeTure M, Ramsden M, McGowan E, Forster C, Yue M, Orne J, Janus C, Mariash A, Kuskowski M, Hyman B, Hutton M, Ashe KH (2005) Tau suppression in a neurodegenerative mouse model improves memory function. *Science* **309**, 476-481.

[11] Hutton M, Lendon CL, Rizzu P, Baker M, Froelich S, Houlden H, Pickering-Brown S, Chakraverty S, Isaacs A, Grover A, Hackett J, Adamson J, Lincoln S, Dickson D, Davies P, Petersen RC, Stevens M, de Graaff E, Wauters E, van Baren J, Hillebrand M, Joosse M, Kwon JM, Nowotny P, Che LK, Norton J, Morris JC, Reed LA, Trojanowski J, Basun H, Lannfelt L, Neystat M, Fahn S, Dark F, Tannenberg T, Dodd PR, Hayward N, Kwok JB, Schofield PR, Andreadis A, Snowden J, Craufurd D, Neary D, Owen F, Oostra BA, Hardy J, Goate A, van Swieten J, Mann D, Lynch T, Heutink P (1998) Association of missense and 5'-splice-site mutations in tau with the inherited dementia FTDP-17. *Nature* **393**, 702-705.

[12] Berger Z, Roder H, Hanna A, Carlson A, Rangachari V, Yue M, Wszolek Z, Ashe K, Knight J, Dickson D, Andorfer C, Rosenberry TL, Lewis J, Hutton M, Janus C (2007) Accumulation of pathological tau species and memory loss in a conditional model of tauopathy. *J Neurosci* **27**, 3650-3662.

[13] Kopeikina KJ, Polydoro M, Tai HC, Yaeger E, Carlson GA, Pitstick R, Hyman BT, Spires-Jones TL (2013) Synaptic alterations in the rTg4510 mouse model of tauopathy. *J Comp Neurol* **521**, 1334-1353.

[14] Barten DM, Fanara P, Andorfer C, Hoque N, Wong PY, Husted KH, Cadelina GW, Decarr LB, Yang L, Liu V, Fessler C, Protassio J, Riff T, Turner H, Janus CG, Sankaranarayanan S, Polson C, Meredith JE, Gray G, Hanna A, Olson RE, Kim SH, Vite GD, Lee FY, Albright CF (2012) Hyperdynamic microtubules, cognitive deficits, and pathology are improved in tau transgenic mice with low doses of the microtubule-stabilizing agent BMS-241027. *J Neurosci* **32**, 7137-7145.

[15] Sahara N, DeTure M, Ren Y, Ebrahim AS, Kang D, Knight J, Volbracht C, Pedersen JT, Dickson DW, Yen SH, Lewis J (2013) Characteristics of TBS-extractable hyperphosphorylated tau species: Aggregation intermediates in rTg4510 mouse brain. *J Alzheimers Dis* **33**, 249-263.

[16] Ramsden M, Kotilinek L, Forster C, Paulson J, McGowan E, SantaCruz K, Guimaraes A, Yue M, Lewis J, Carlson G, Hutton M, Ashe KH (2005) Age-dependent neurofibrillary tangle formation, neuron loss, and memory impairment in a mouse model of human tauopathy (P301L). *J Neurosci* **25**, 10637-10647.

[17] Dickey C, Kraft C, Jinwal U, Koren J, Johnson A, Anderson L, Lebson L, Lee D, Dickson D, de Silva R, Binder LI, Morgan D, Lewis J (2009) Aging analysis reveals slowed tau turnover and enhanced stress response in a mouse model of tauopathy. *Am J Pathol* **174**, 228-238.

[18] Fontaine SN, Ingram A, Cloyd RA, Meier SE, Miller E, Lyons D, Nation GK, Mechas E, Weiss B, Lanzillotta C, Di Domenico F, Schmitt F, Powell DK, Vandsburger M, Abisambra JF (2017) Identification of changes in neuronal function as a consequence of aging and tauopathic neurodegeneration using a novel and sensitive magnetic resonance imaging approach. *Neurobiol Aging* **56**, 78-86.

[19] Majid T, Ali YO, Venkitaramani DV, Jang MK, Lu HC, Pautler RG (2014) In vivo axonal transport deficits in a mouse model of fronto-temporal dementia. *Neuroimage Clin* **4**, 711-717.

[20] Perez PD, Hall G, Kimura T, Ren Y, Bailey RM, Lewis J, Febo M, Sahara N (2013) In vivo functional brain mapping in a conditional mouse model of human tauopathy (taup301l) reveals reduced neural activity in memory formation structures. *Mol Neurodegener* **8**, 9.

[21] Fodero-Tavoletti MT, Okamura N, Furumoto S, Mulligan RS, Connor AR, McLean CA, Cao D, Rigopoulos A, Cartwright GA, O'Keefe G, Gong S, Adlard PA, Barnham KJ, Rowe CC, Masters CL, Kudo Y, Cappai R, Yanai K, Villemagne VL (2011) 18F-THK523: A novel *in vivo* tau imaging ligand for Alzheimer's disease. *Brain* **134**, 1089-1100.

[22] Holmes HE, Colgan N, Ismail O, Ma D, Powell NM, O'Callaghan JM, Harrison IF, Johnson RA, Murray TK, Ahmed Z, Heggenes M, Fisher A, Cardoso MJ, Modat M, Walker-Samuel S, Fisher EM, Ourselin S, O'Neill MJ, Wells JA, Collins EC, Lythgoe MF (2016) Imaging the accumulation and suppression of tau pathology using multiparametric MRI. *Neurobiol Aging* **39**, 184-194.

[23] Gerhard A, Watts J, Trender-Gerhard I, Turkheimer F, Banati RB, Bhatia K, Brooks DJ (2004) In vivo imaging of microglial activation with [11C](R)-PK11195 PET in corticobasal degeneration. *Mov Disord* **19**, 1221-1226.

[24] Gerhard A, Trender-Gerhard I, Turkheimer F, Quinn NP, Bhatia KP, Brooks DJ (2006) In vivo imaging of microglial activation with [11C](R)-PK11195 PET in progressive supranuclear palsy. *Mov Disord* **21**, 89-93.

[25] Wyss-Coray T (2006) Inflammation in Alzheimer disease: Driving force, bystander or beneficial response? *Nat Med* **12**, 1005-1015.

[26] Yoshiyama Y, Higuchi M, Zhang B, Huang SM, Iwata N, Saido TC, Maeda J, Suhara T, Trojanowski JQ, Lee VM (2007) Synapse loss and microglial activation precede tangles in a P301S tauopathy mouse model. *Neuron* **53**, 337-351.

[27] Diorio D, Welner SA, Butterworth RF, Meaney MJ, Suranyi-Cadotte BE (1991) Peripheral benzodiazepine binding sites in Alzheimer's disease frontal and temporal cortex. *Neurobiol Aging* **12**, 255-258.

[28] Janssen B, Vugts DJ, Funke U, Molenaar GT, Kruijer PS, van Berckel BN, Lammertsma AA, Windhorst AD (2016) Imaging of neuroinflammation in Alzheimer's disease, multiple sclerosis and stroke: Recent developments in positron emission tomography. *Biochim Biophys Acta* **1862**, 425-441.

[29] Yasuno F, Ota M, Kosaka J, Ito H, Higuchi M, Doronbekov TK, Nozaki S, Fujimura Y, Koeda M, Asada T, Suhara T (2008) Increased binding of peripheral benzodiazepine receptor in Alzheimer's disease measured by positron emission tomography with [11C]DAA1106. *Biol Psychiatry* **64**, 835-841.

[30] Maeda J, Zhang MR, Okauchi T, Ji B, Ono M, Hattori S, Kumata K, Iwata N, Saido TC, Trojanowski JQ, Lee VM, Staufenbiel M, Tomiyama T, Mori H, Fukumura T, Suhara T, Higuchi M (2011) In vivo positron emission tomographic imaging of glial responses to amyloid-beta and tau pathologies in mouse models of Alzheimer's disease and related disorders. *J Neurosci* **31**, 4720-4730.

[31] Paxinos G, Franklin KBJ (2004) *The Mouse Brain in Stereotaxic Coordinates*, 2nd edition. Gulf Professional Publishing.

[32] Tai YC, Laforest R (2005) Instrumentation aspects of animal PET. *Annu Rev Biomed Eng* **7**, 255-285.

[33] Hashimoto H, Kawamura K, Igarashi N, Takei M, Fujishiro T, Aihara Y, Shiomi S, Muto M, Ito T, Furutsuka K, Yamasaki T, Yui J, Xie L, Ono M, Hatori A, Nemoto K, Suhara T, Higuchi M, Zhang MR (2014) Radiosynthesis, photoisomerization, biodistribution, and metabolite analysis of 11C-PBB3 as a clinically useful PET probe for imaging of tau pathology. *J Nucl Med* **55**, 1532-1538.

[34] Zhang MR, Kumata K, Maeda J, Yanamoto K, Hatori A, Okada M, Higuchi M, Obayashi S, Suhara T, Suzuki K (2007) 11C-AC-5216: A novel PET ligand for peripheral benzodiazepine receptors in the primate brain. *J Nucl Med* **48**, 1853-1861.

[35] Yang D, Xie Z, Stephenson D, Morton D, Hicks CD, Brown TM, Sriram R, O'Neill S, Raunig D, Bocan T (2011) Volumetric MRI and MRS provide sensitive measures of Alzheimer's disease neuropathology in inducible Tau transgenic mice (rTg4510). *Neuroimage* **54**, 2652-2658.

[36] Maeda J, Ji B, Irie T, Tomiyama T, Maruyama M, Okauchi T, Staufenbiel M, Iwata N, Ono M, Saido TC, Suzuki K, Mori H, Higuchi M, Suhara T (2007) Longitudinal, quantitative assessment of amyloid, neuroinflammation, and anti-amyloid treatment in a living mouse model of Alzheimer's disease enabled by positron emission tomography. *J Neurosci* **27**, 10957-10968.

[37] Bailey RM, Howard J, Knight J, Sahara N, Dickson DW, Lewis J (2014) Effects of the C57BL/6 strain background on tauopathy progression in the rTg4510 mouse model. *Mol Neurodegener* **9**, 8.

[38] Spires TL, Orne JD, SantaCruz K, Pitstick R, Carlson GA, Ashe KH, Hyman BT (2006) Region-specific dissociation of neuronal loss and neurofibrillary pathology in a mouse model of tauopathy. *Am J Pathol* **168**, 1598-1607.

[39] Sahara N, Ren Y, Ward S, Binder LI, Suhara T, Higuchi M (2014) Tau oligomers as potential targets for early diagnosis of tauopathy. *J Alzheimers Dis* **40**(Suppl 1), S91-96.

[40] Grober E, Dickson D, Sliwinski MJ, Buschke H, Katz M, Crystal H, Lipton RB (1999) Memory and mental status correlates of modified Braak staging. *Neurobiol Aging* **20**, 573-579.

[41] Riley KP, Snowdon DA, Markesbery WR (2002) Alzheimer's neurofibrillary pathology and the spectrum of cognitive function: Findings from the Nun Study. *Ann Neurol* **51**, 567-577.

[42] Barron M, Gartlon J, Dawson LA, Atkinson PJ, Pardon MC (2017) A state of delirium: Deciphering the effect of inflammation on tau pathology in Alzheimer's disease. *Exp Gerontol* **94**, 103-107.

[43] Higuchi M, Ji B, Maeda J, Sahara N, Suhara T (2016) In vivo imaging of neuroinflammation in Alzheimer's disease. *Clin Exp Neuroimmunol* **7**, 139-144.

[44] Sy M, Kitazawa M, Medeiros R, Whitman L, Cheng D, Lane TE, Laferla FM (2011) Inflammation induced by infection potentiates tau pathological features in transgenic mice. *Am J Pathol* **178**, 2811-2822.

[45] Ghosh S, Wu MD, Shaftel SS, Kyrkanides S, LaFerla FM, Olschowka JA, O'Banion MK (2013) Sustained interleukin-1beta overexpression exacerbates tau pathology despite reduced amyloid burden in an Alzheimer's mouse model. *J Neurosci* **33**, 5053-5064.

[46] Lee DC, Rizer J, Selenica ML, Reid P, Kraft C, Johnson A, Blair L, Gordon MN, Dickey CA, Morgan D (2010) LPS-induced inflammation exacerbates phospho-tau pathology in rTg4510 mice. *J Neuroinflammation* **7**, 56.

[47] in t' Veld BA, Ruitenberg A, Hofman A, Launer LJ, van Duijn CM, Stijnen T, Breteler MM, Stricker BH (2001) Nonsteroidal antiinflammatory drugs and the risk of Alzheimer's disease. *N Engl J Med* **345**, 1515-1521.

[48] Brugg B, Dubreuil YL, Huber G, Wollman EE, Delhaye-Bouchaud N, Mariani J (1995) Inflammatory processes induce beta-amyloid precursor protein changes in mouse brain. *Proc Natl Acad Sci U S A* **92**, 3032-3035.

[49] Fiala M, Cribbs DH, Rosenthal M, Bernard G (2007) Phagocytosis of amyloid-beta and inflammation: Two faces of innate immunity in Alzheimer's disease. *J Alzheimers Dis* **11**, 457-463.

[50] Yamin G, Teplow DB (2017) Pittsburgh Compound-B (PiB) binds amyloid beta-protein protofibrils. *J Neurochem* **140**, 210-215.

[51] Wischik CM, Edwards PC, Lai RY, Roth M, Harrington CR (1996) Selective inhibition of Alzheimer disease-like tau aggregation by phenothiazines. *Proc Natl Acad Sci U S A* **93**, 11213-11218.

[52] Bolognesi B, Kumita JR, Barros TP, Esbjorner EK, Luheshi LM, Crowther DC, Wilson MR, Dobson CM, Favrin G, Yerbury JJ (2010) ANS binding reveals common features of cytotoxic amyloid species. *ACS Chem Biol* **5**, 735-740.

[53] Smith NW, Alonso A, Brown CM, Dzyuba SV (2010) Triazole-containing BODIPY dyes as novel fluorescent probes for soluble oligomers of amyloid Abeta1-42 peptide. *Biochem Biophys Res Commun* **391**, 1455-1458.

[54] Jameson LP, Dzyuba SV (2013) Aza-BODIPY: Improved synthesis and interaction with soluble Abeta1-42 oligomers. *Bioorg Med Chem Lett* **23**, 1732-1735.

[55] Teoh CL, Su D, Sahu S, Yun SW, Drummond E, Prelli F, Lim S, Cho S, Ham S, Wisniewski T, Chang YT (2015) Chemical fluorescent probe for detection of Abeta oligomers. *J Am Chem Soc* **137**, 13503-13509.